A dynamic micro-CT scanner based on a carbon nanotube field emission x-ray source

G Cao[1], Y Z Lee[1,2], R Peng[3], Z Liu[1,7], R Rajaram[3], X Calderon-Colon[3], L An[1], P Wang[1], T Phan[4], S Sultana[3], D S Lalush[5], J P Lu[1,3] and O Zhou[1,3,6]

[1] Department of Physics and Astronomy, University of North Carolina, Chapel Hill, NC 27599, USA
[2] Department of Radiology, University of North Carolina, Chapel Hill, NC 27599, USA
[3] Curriculum in Applied Sciences and Engineering, University of North Carolina, Chapel Hill, NC 27599, USA
[4] Department of Biomedical Engineering, University of North Carolina, Chapel Hill, NC 27599, USA
[5] Department of Biomedical Engineering, North Carolina State University, Raleigh, NC 27695, USA
[6] Lineberger Comprehensive Cancer Center, University of North Carolina, Chapel Hill, NC 27599, USA

E-mail: gcao@physics.unc.edu and zhou@physics.unc.edu

Abstract

Current commercial micro-CT scanners have the capability of imaging objects *ex vivo* with high spatial resolution, but performing *in vivo* micro-CT on free-breathing small animals is still challenging because their physiological motions are *non-periodic* and much faster than those of humans. In this paper, we present a prototype physiologically gated micro-computed tomography (micro-CT) scanner based on a carbon nanotube field emission micro-focus x-ray source. The novel x-ray source allows x-ray pulses and imaging sequences to be readily synchronized and gated to *non-periodic* physiological signals from small animals. The system performance is evaluated using phantoms and sacrificed and anesthetized mice. Prospective respiratory-gated micro-CT images of anesthetized free-breathing mice were collected using this scanner at 50 ms temporal resolution and 6.2 lp mm^{-1} at 10% system MTF. The high spatial and temporal resolutions of the micro-CT scanner make it well suited for high-resolution imaging of free-breathing small animals.

[7] Present address: Department of Radiation Oncology and Molecular Radiation Sciences, School of Medicine, Johns Hopkins University, Baltimore, MD 21231, USA.

1. Introduction

Micro-computed tomography (micro-CT) is an important tool in non-invasive screening of small animals such as mice and rats for pre-clinical cancer studies (Paulus *et al* 2000, Holdsworth and Thornton 2002, Ritman 2004). Current commercially available preclinical micro-CT scanners offer the capability of imaging objects *ex vivo* with high spatial resolution on the order of 10 μm (Paulus *et al* 2000), but performing *in vivo* micro-CT on small animals is still challenging largely because their physiological motions are much faster than those of humans. Motion-induced artifacts blur the micro-CT images resulting in significantly deteriorated spatial resolution.

Previously it had been shown that artifacts resulted from respiration motion can be minimized by techniques such as restricting the motion through applying a sticky tape around the chest (De Clerck *et al* 2004) and retrospective gating where projections were taken without gating but only the images belonging to a retrospectively selected respiratory phase were reconstructed (Hu *et al* 2004, Ford *et al* 2007b, Drangova *et al* 2007). It had also been reported that respiratory motion can be minimized by an intermittent iso-pressure breath hold (IIBH) technique which can almost completely freeze the respiratory motion during image acquisition and produce greater image resolution (Namati *et al* 2006). There had been numerous other methods proposed for reducing the motion artifacts through prospective gating techniques where the image acquisitions were synchronized with the physiological signals. In those methods, animals were either intubated and ventilator controlled (Hedlund and Johnson 2002, Badea *et al* 2004, Cavanaugh *et al* 2004, Walters *et al* 2004, Cody *et al* 2005, Nahrendorf *et al* 2007) or free breathing (Ford *et al* 2005, 2007a). Intubation requires dedicated equipment and special animal handling skills to avoid damage to the upper airways (Brown *et al* 1999). The respiratory mechanics and lung function of the animal could be altered from paralysis (Hirai *et al* 1999). In addition, when animals were ventilator controlled, the pressure and volume settings can affect the morphology and mechanics, thereby making true measurements of function and structure difficult to obtain (Nilsson 1979, Nilsson *et al* 1980, Gomes *et al* 2001, Nakamura *et al* 2001).

Micro-CT imaging of free-breathing animals is preferred for longitudinal studies and for disease models where mechanical ventilation may introduce systematic errors into the physiologically relevant measurements. Imaging of free-breathing rodents using retrospective gating technique had been reported (Hu *et al* 2004, Ford *et al* 2007b). Although the retrospective gating technique can image the entire breathing cycle at the same dosage as that of normal methods, it unavoidably requires redundant projections/exposures to minimize the missing view artifact if only one phase in the breathing cycle is to be imaged. Imaging of free-breathing rodents had also been done with prospective gating technique using commercial micro-CT scanners (Ford *et al* 2005, 2007a). Because of the time interval required for the x-ray shutter to open and close, the *effective* temporal resolution was limited at 170 ms. This temporal resolution is not sufficient to precisely define the peak inspiration phase in a mouse. In addition, each projection image had to be averaged from up to 10 frames in order to achieve a good image quality. The reported total scan time is 20–25 min.

Our objective, therefore, is to develop a dynamic micro-CT scanner with enhanced temporal and spatial resolution that are sufficient to resolve the cardiopulmonary organs of free-breathing mice. The key to our approach is the new carbon nanotube (CNT) field emission micro-focus x-ray source technology. The novel x-ray source utilizes a CNT film as the 'cold' electron gun to generate x-ray radiation. The source can be operated in the energy range of 40–60 kVp with an effective focal spot size down to 30 μm (Liu *et al* 2006). At a given CNT cathode size, the x-ray focal spot size can be adjusted within a certain range
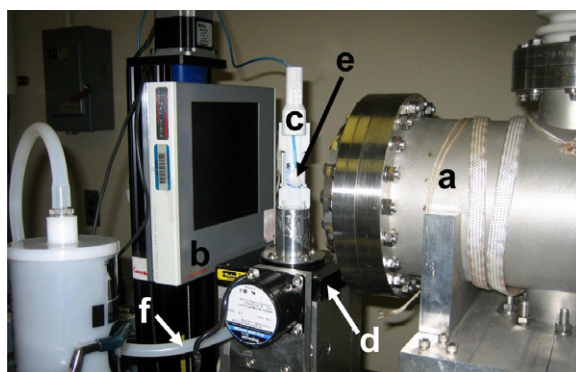
Figure 1. The CNT x-ray source (a) and camera (b) are stationary. The mouse is mounted vertically in a custom-built sample holder (c) which is rotated by a computer-controlled rotation stage (d). The sample holder and the rotation stage together form the sample stage. The source, detector and sample stage are supported on a pneumatic-isolators equipped optical table to limit the impact of floor vibration. The relative positions of the detector and sample stage can be easily adjusted through stepping motors. The respiration sensor (e) is attached to the abdomen of mouse from the top of the sample holder. The anesthesia gas (f) is delivered from a vaporizer to a specially made gas tank underneath the acrylic mouse holder with an open-end nose cone.

with electrostatic focusing. The x-ray waveform can be readily programed and synchronized to an external triggering signal with microsecond temporal resolution and minimum delay (Cheng *et al* 2004). Compared to the micro-focused x-ray tubes currently used for micro-CT where switching on and off the x-ray radiation is still performed by a mechanical shutter (Ford *et al* 2005, Namati *et al* 2006), this is desirable for gated imaging of live animals where the physiological motions are *non-periodic*.

In this paper, we present a research prototype dynamic micro-CT scanner based on the CNT field emission micro-focus x-ray source. The focal spot size, flux and stability of the CNT x-ray source were evaluated. The quantitative performance parameters of the scanner including system MTF, temporal resolution, contrast-to-noise ratio (CNR) and linearity were characterized and discussed. System performance was evaluated by feasibility studies in high-resolution micro-CT of a sacrificed mouse and in prospective respiratory-gated micro-CT of several anesthetized free-breathing mice.

2. Materials and methods

2.1. Overview of the micro-CT scanner

Figure 1 shows a picture of the dynamic volumetric micro-CT scanner with a micro-focus CNT x-ray source and a flat-panel detector arranged in the cone-beam geometry. In this design, the CNT x-ray source and the x-ray camera are stationary while the sample is rotated. The design, fabrication and performance of the CNT x-ray source are described in subsection 2.3. The camera is placed as close to the x-ray source as possible to maximize the amount of imaging flux. The animal is suspended vertically in a custom-built sample holder that is locked to a metal support attached to a computer-controlled rotation stage. The camera is a high-speed CMOS flat-panel sensor with a CsI scintillator plate directly deposited on a photo diode array (Model C7940DK-02, Hamamatsu). It has 2400×2400 pixels with a nominal pixel size of 50 μm, giving an active area of 120×120 mm^2. It has a thin carbon fiber

cover and allows flexible readout and rebinning. For this study, the camera was configured to utilize only about one-fourth of its full field-of-view (FOV) at the central region without binning, producing two-dimensional 1024×1024 projection images at $50 \times 50\,\mu m^2$ pixel resolution. The cone-beam geometry was determined using a two-ball phantom following the procedure outlined by Noo *et al* (2000). The source-to-object distance was found to be 135 mm. The source-to-detector distance was 216 mm, hence the magnification factor was 1.6, the cone angle was $14°$ and the FOV of the scanner was determined to be 32×32 mm^2.

The micro-CT scanner has versatile imaging capabilities. It can be used to do both gated and non-gated micro-CT scans on small animals or specimens. For gated micro-CT scans, the scanner followed a dynamic gating scheme described in subsection 2.2. For non-gated micro-CT scans, the scanner acquired projection images one after another disregard to the physiological trigger signal. There was always an x-ray pulse fired in every x-ray exposure window defined in figure 2(b). A computer program was developed using LabVIEW (National Instruments, Austin, TX, USA) to handle the task of synchronizing the x-ray pulse firing to the camera frame acquisition and also to the physiological triggers if it was a gated scan. This program also controls the rotation of the sample through a RS-232 interface to a Velmex VXM stepping motor (Velmex, Inc., Bloomfield, NY, USA). The scanner allows users to select the x-ray pulse width (1 μs–10 s) and the camera frame rate (0.1–2 frames per second at 1×1 binning mode). It also allows multiple frame acquisition at each projection view.

The standard scanning parameters, unless otherwise noted, were 40 kVp, 0.7 mA anode current, 50 ms x-ray pulse width, 325 projections over a circular orbit of $195°$ with a step angle of $0.6°$ and 50 bright and dark calibration images throughout this study. By setting the camera frame rate at 1 frame per second, the total time for projection acquisition of a respiratory-gated micro-CT scan was typically 5–10 min depending on the mouse respiration rate. For a non-gated micro-CT scan, the total time was simply the product of the camera frame rate and the total number of projections. For example, the total time for a specimen scan would be 5 min if the camera frame rate was set at 1 frame per second and a total of 325 projections were acquired. Images were reconstructed with a modified Feldkamp algorithm (Feldkamp *et al* 1984) using a commercial software package (Cobra EXXIM, Exxim Computing Corp., Livermore, CA, USA). Although our geometry configuration could give an effective digital sampling in the object plane of 31 μm, data from a respiratory-gated micro-CT scan were reconstructed as isotropic $512 \times 512 \times 512$ arrays with a voxel size of $62 \times 62 \times 62\,\mu m^3$. On a single PC with a 2.8 GHz dual-core CPU, the reconstruction time was about 3 min.

2.2. The dynamic gating

Figure 2 shows the schematics of the micro-CT scanner and its timing diagram for respiratory-gated micro-CT of free-breathing mice. The timing diagram is what the controlling computer used to gate the x-ray pulse firing and the camera frame acquisition to the physiological signal from a mouse. The camera runs on a continuous, pre-defined frame rate. For this study, the camera was configured at 1×1 binning mode and had a 470 ms readout time, thus the maximum allowable frame rate at this mode was 2 frames per second. The camera frame rate, camera readout time and the x-ray pulse width together determine the x-ray exposure window. The exposure window is defined as the time window between the end of a previous frame readout and the beginning of next frame readout subtracted by the x-ray pulse width, t_{pw}. This subtraction is to ensure that the x-ray pulse would not over extend into the camera readout region. The respiration signal and the physiological trigger were obtained using an animal physiological monitoring system (BioVet, Spin Systems (QLD) Pty Ltd, Brisbane, Australia). The dynamic gating was achieved from the logic AND operation between the exposure window
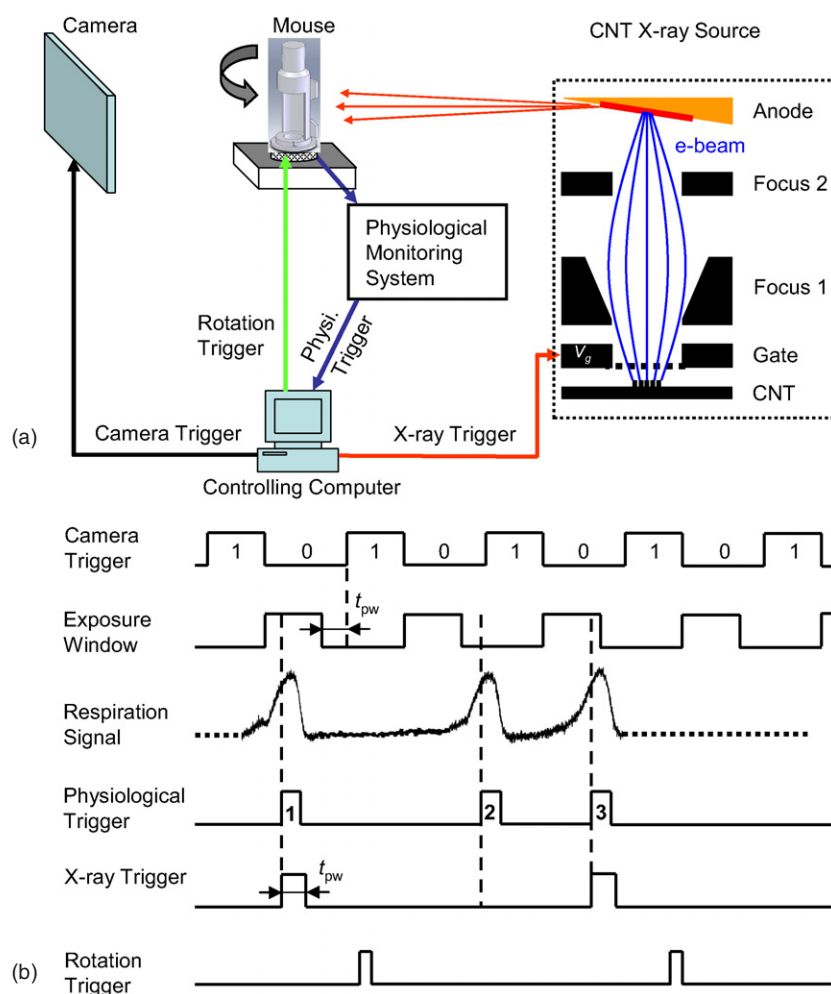
Figure 2. (a) Schematics of the micro-CT scanner. The scanner is fully automated by a controlling computer that runs LabVIEW. The controlling computer monitors the physiological trigger signal from a mouse and gates it to the x-ray exposure window of the scanner through a home-built digital electronic circuit. If the gating condition is satisfied, the controlling computer sends out the x-ray trigger that controls the x-ray pulse firing and the camera trigger that controls the image acquisition. The controlling computer also instructs the rotation stage to rotate the sample between projection views. (b) Illustrative timing diagram that the controlling computer used to gate the x-ray pulse firing and the camera frame acquisition to the respiration signal. The camera readout and integration regions are designated as 1 and 0, respectively. t_{pw} is the temporal width of an x-ray pulse.

signal and the physiological trigger signal by an AND transistor-to-transistor logic (TTL) gate. The output of this AND gate was used as the trigger to generate the x-ray trigger signal that controls the x-ray pulse firing. An x-ray trigger pulse was enabled only by the rising edge of a TTL pulse outputted from the logic AND gate. The physiological triggers generated from the respiration signal of a free-breathing mouse can be *non-periodic*, such as the three physiological triggers shown in figure 2(b). The rising edges of the physiological triggers 1 and 3 come within the x-ray exposure window, thus they will each trigger an x-ray pulse. On
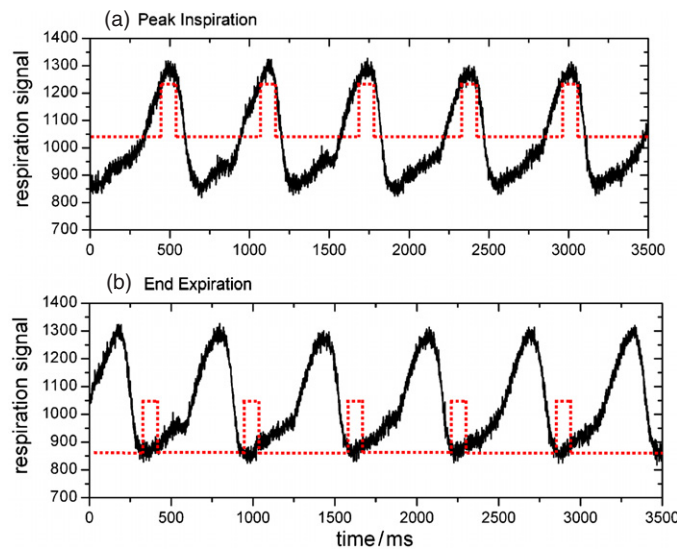
Figure 3. Representative samples of the respiration signals from the Biovet physiological monitoring system with the corresponding physiological triggers (red dotted squares) superimposed at the corresponding phase portions of the respiration cycles. These physiological triggers are gated with the exposure windows to generate the x-ray triggers, as illustrated in figure 2(b). X-ray imaging windows were 50 ms in duration for both peak inspiration (a) and end expiration (b).

the other hand, the physiological trigger 2 will not trigger an x-ray pulse because its rising edge is outside the x-ray exposure window. In conclusion, x-rays are fired on demand. This 'fire-on-demand' of the timing scheme intrinsically enables a high-dose efficiency. It is worth to point out that x-ray firings are based on temporal coincidence between the x-ray exposure window and the physiological triggers. The total scan time for a dynamically gated scan depends on the rate of this temporal coincidence.

The selection of different respiratory phases is shown in figure 3. The diaphragm motion induced a pressure change in the respiration sensor, which was detected by a pressure transducer to give the respiration signal. The physiological triggers were generated once the respiration signal rose above a high-threshold level or fell below a low-threshold level, for imaging gated at peak inspiration or end expiration, respectively. Both threshold levels were manually selected prior to image acquisitions. For images acquired at peak inspiration, the physiological triggers were positioned such that a 50 ms windows straddling the peak (figure 3(a)); and for images acquired at end expiration, the physiological triggers were positioned at the beginning of the plateau between breaths (figure 3(b)). The physiological triggers can be delayed to coincide with any portion of the respiratory cycle and used to trigger the image acquisition. The x-ray pulse width, hence the frame exposure, was selected at 50 ms to balance the exposure for each projection image and the degradation of resolution arising from respiratory motion.

2.3. The CNT-based field emission micro-focus x-ray source

The key to this *in vivo* micro-CT scanner with enhanced spatial and temporal resolutions is to develop a micro-focus x-ray source with small focal spot size and high flux. For a conventional x-ray source the x-ray power is primarily limited by heat dissipation of the x-ray anode. At present, the flux of a CNT-based micro-focus x-ray source has not yet reached the limit set by the x-ray anode because of limitation on the maximum emission current density (current

per unit cathode area) that can be stably and reliably obtained from a CNT cathode. In our laboratory this value is $\sim$0.1 A cm^{-2}, which is a moving target that will be increased with further improvement in the cathode fabrication process. We have previously shown that the focal diameter is linearly dependent on the CNT cathode diameter (Liu *et al* 2006). This means that the smaller the focal spot size, the smaller the CNT cathode and thus the lower the x-ray tube current. With this constrain in mind, it is important to design the x-ray source with balanced focal spot size and flux and the scanner with a balanced spatial and temporal resolutions. In this study, we have targeted $\sim$100 μm isotropic focal spot size which would result in a system resolution of $\sim$80 μm with the targeted system geometry, sufficient to resolve mouse cardiopulmonary organs.

The electron focusing design of the CNT x-ray source employed in this study is similar to our previous work (Liu *et al* 2006) with slight modifications. The CNT cathode has an elliptical area of 2.35 mm $\times$ 0.5 mm. The anode tilting angle was set to 12°. Electron trajectory simulation using a commercial software package (Opera, Vector Fields Inc., Aurora, IL, USA) showed that an optimum focusing factor of about 5 could be obtained. Therefore, after projection by the anode tilting angle, the *effective* focal spot size would be 100 μm $\times$ 100 μm. The CNT cathode was fabricated using a previously published electrophoretic deposition method developed in our lab (Oh *et al* 2004). The entire x-ray source was housed inside a vacuum chamber with a 200 μm thick beryllium foil as the x-ray exit window.

The CNT x-ray source could be reliably operated at 0.7 mA anode current and 40 kV anode voltage, i.e., 28 W tube power. The effective focal spot was measured following the European standard EN 12543-5 (European Committee for Standardization 1999) by using a cross wire phantom consisting of two 1 mm diameter tungsten wires in two orthogonal directions. The optimum effective focal spot was found to be $117 \times 117 \, \mu$m^2. The source was running with heavy use for $\sim$160 days before failure. The total electron beam on time during the lifetime of the source was estimated to be $\sim$20 h.

### 2.4. System performance characterization

2.4.1. MTF analysis. A 10 μm tungsten wire phantom (QRM, Nuremburg, Germany) was used to characterize the modulation transfer function (MTF) of the micro-CT scanner. The tungsten wire was positioned nearly parallel (less than 2°) to the rotation axis. The phantom was scanned with the standard scanning parameters and reconstructed with a voxel size of $10 \times 10 \times 10 \, \mu$m^3.

After reconstruction, the system MTF was calculated based on a similar method described by Kwan *et al* (2007). For each reconstructed CT slice, the line-spread function (LSF) was received from integrating a small (39 $\times$ 79 pixels) region of interest (ROI) around the wire as illustrated in figure 4. The center of the mass along the x-axis direction (CM$_x$) for each LSF was computed as

$$\mathrm{CM}_x = \sum_x \sum_y (I(x, y) \times x] \Big/ \sum_x \sum_y I(x, y), \tag{1}$$

where $I(x, y)$ is the pixel intensity at spatial coordinate (x, y) within the ROI. The CM for all the LSFs in a given reconstructed volume data set were plotted as a function of the slice number and fitted with linear regression. The resulting regression parameters were used to determine the LSF centers along the CT slices, which were then used for over sampling the LSF with a similar method proposed by Fujita *et al* (1992). The over-sampled LSF was rebinned and averaged to reduce noise and finally Fourier transformed to receive the system MTF.
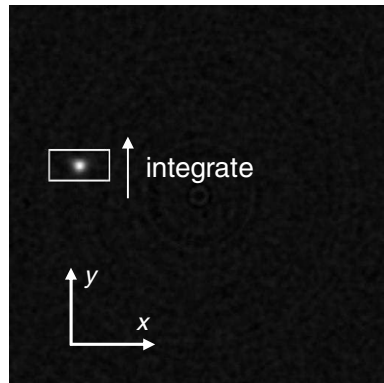
Figure 4. An illustration of the reconstructed 10 μm tungsten wire phantom image is shown. The ROI (white box) is 39 × 79 pixels, and was integrated in the *y*-axis direction to produce the LSF needed for the MTF calculation.

2.4.2. Contrast-to-noise ratio. The contrast and noise of the micro-CT scanner were examined by scanning a 25 mm diameter acrylic cylindrical phantom (hereafter referred as the contrast phantom) containing five 5 mm diameter cylindrical cavities drilled evenly along a concentric circle of 15 mm diameter. The contrast phantom was 30 mm long and the cavities were 25 mm deep. Each cavity was filled with air, water, fat mimic (soybean oil with 22% fat), diluted contrast agent (30 mgI mL^{-1}, OMNIPAQUE^{TM}, GE Healthcare) and bone simulator (powder hydroxyapatite, Sigma-Aldrich, St. Louis, MO, USA), respectively. This tissue-equivalent phantom was scanned with the standard scanning parameters. Projection data were reconstructed as isotropic 512 × 512 × 512 arrays with a voxel size of 62 × 62 × 62 μm^3. The average and standard deviation of the pixel values within a 3 × 3 × 3 mm^3 ROI placed manually in the center of each material sample were calculated to show the system's contrast and noise levels. Pixel values were scaled to Hounsfield units by setting the average pixel values within water and air ROIs to 0 and −1000 HU, respectively. The CNRs between water and air and between water and oil were calculated. The CNR between substance 1 and substance 2 is defined by the following equation (Tward *et al* 2007):

$$\text{CNR}_{1,2} = \frac{\mu_1 - \mu_2}{(\sigma_1 + \sigma_2)/2}, \tag{2}$$

where μ_1, μ_2 and σ_1, σ_2 are the averages and standard deviations of the pixel values from the ROIs contained within the images of substance 1 and substance 2, respectively.

2.4.3. Linearity. The linearity of the micro-CT scanner was investigated by scanning a 30 mm diameter acrylic cylindrical phantom (hereafter referred to as the linearity phantom) containing seven 5 mm diameter cylindrical cavities drilled evenly along a concentric circle of 20 mm diameter. The linearity phantom was 30 mm long and the cavities were 25 mm deep. Two of those cavities were filled with water and air, and the remaining five cavities were each filled with different concentration of iodine contrast agent solutions in 1.175, 3.25, 7.5, 15 and 30 mgI mL^{-1}, respectively. The 30 mgI mL^{-1} solution was prepared by diluting 2.0 ml of full-strength nonionic iohexol contrast material (OMNIPAQUE^{TM} 300 mgI mL^{-1}, GE Healthcare) with 18.0 ml of distilled water. To make the 15 mgI mL^{-1} solution, 5.0 ml of the 30 mgI mL^{-1} solution was diluted with 5.0 ml of distilled water. This 1:1 dilution process was repeated three more times to make the rest of the iodine solutions.
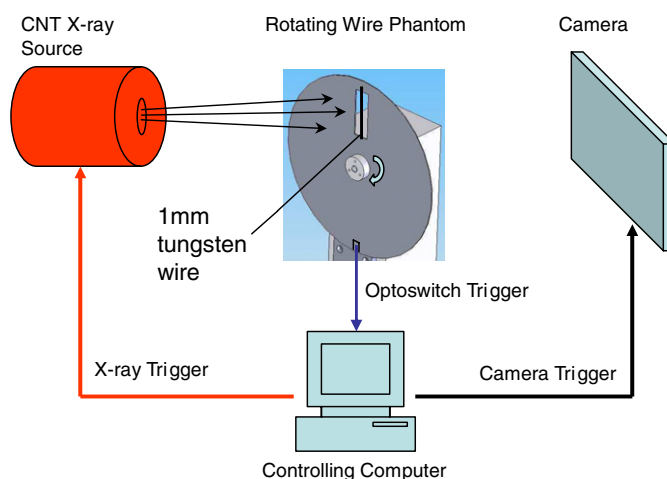
Figure 5. The experiment setup for the system temporal analysis using the rotating wire phantom.

The linearity phantom was scanned with the standard scanning parameters. Projection data were reconstructed as isotropic $512 \times 512 \times 512$ arrays with a voxel size of $62 \times 62 \times 62 \, \mu m^3$. The average pixel values for water, air and various iodine concentrations were measured, within a $2 \times 2 \times 2 \, mm^3$ ROI placed manually in the center of each cavity, respectively. The average pixel values from the five iodine concentrations were scaled to Hounsfield units by setting the average reading from the air ROI to -1000 HU and the average reading from the water ROI to 0 HU. The relationship between signal intensity and iodine concentration was determined by linear regression analysis.

2.4.4. Temporal analysis. The temporal response of the micro-CT scanner was analyzed with a rotating wire phantom. In this phantom, a 1 mm diameter tungsten wire was mounted radially across a 20 mm $\times$ 60 mm cut-out section of a 1 mm thick aluminum disc with a radius of 115 mm. The aluminum disc was mounted on a stable rotor with manually adjustable speeds. A 3 mm $\times$ 5 mm notch was carved out on the disc's edge opposite to the tungsten wire to serve as the optoswitch trigger point. During the operation, the phantom was put on the sample stage between the source and the camera. A generic optoswitch with a 3 mm slot was coupled to the bottom edge of the disc so that a TTL pulse was generated once the optoswitch trigger point of the disc passed through the optoswitch. This TTL signal generated from the optoswitch replaced the physiological trigger signal during a live mouse scan to trigger the x-ray pulse firing following the same timing diagram shown in figure 2, except that no rotation trigger would be generated to rotate the sample stage. Thus an x-ray image would be taken only when the wire was passing in front of the x-ray detector vertically. The x-ray source was operated at 40 kV and 0.7 mA anode current. An image of the wire was taken at 100 ms pulse width when it was static. Then the images of the moving wire were taken at 100 ms, 50 ms, 20 ms, 10 ms and 5 ms pulse width, respectively. The experiment setup for the system temporal analysis using this rotating wire phantoms is illustrated in figure 5.

2.4.5. Dose measurement. The x-ray dose for a typical micro-CT scan was measured using thermoluminescent dosimeter (TLD). The readout service was provided by K&S Associate,

Inc. (Nashville, TN, USA). TLDs were attached to the skin of a scarified mouse and were exposed during a micro-CT scan following the standard scanning parameters.

2.5. Micro-CT scanning on animals

2.5.1. Micro-CT of an inflated mouse lung in situ. Micro-CT imaging was performed on a sacrificed mouse with an inflated lung. The scanning parameters were 40 kVp, 0.7 mA anode current, 400 ms pulse width, 1 mm aluminum filtratio and 325 views over $195°$. During the scan, the camera frame rate was set to 1 frame per second, thus the total scan time was 5 min. Projection data were reconstructed as isotropic $1024 \times 1024 \times 1024$ arrays with a voxel size of $31 \times 31 \times 31 \mu m^3$. After reconstruction, axial and coronal slices from the volumetric micro-CT data were presented for qualitative assessment. From the presented axial slice, two 20×20 pixels ROIs were manually placed in the heart and trachea, respectively. Averages and standard deviations were found from the pixel values within these two ROIs, and the CNR between the two ROIs was calculated using equation (2). Similarly, CNR between another two 20×20 pixels ROIs manually placed in the heart and chest wall was calculated.

2.5.2. Respiratory-gated micro-CT of free-breathing mice. Respiratory-gated micro-CT imaging was performed on five adult wild-type mice each weighing approximately 25 g. The animals were anesthetized with 1–2% isoflurane at a flow rate of $1.5–2$ L min^{-1} from a vaporizer (Smith Medical PM Inc., Waukesha, WI, USA). The animal breathing rates after anesthetization were typically in the range of 80–180 breathsmin^{-1}. The anesthetized animals were placed over the pressure sensor in the mouse sample holder and secured with adhesive restraints. The animals were positioned such that the respiration sensor was approximately in the position of the abdomen to achieve maximum sensor coupling. Experimental procedures carried out in this study had been approved by University of North Carolina Institutional Animal Care and Use Committee.

Each mouse was scanned with the standard scanning parameters and with respiration gated to the mouse's peak inspiration, followed with another scan gated to its end expiration. With the camera running at 1 frame per second, the scan time was typically 5–10 min depending on the mouse respiration rates. Projection data were reconstructed as isotropic $512 \times 512 \times 512$ arrays with a voxel size of $62 \times 62 \times 62 \mu m^3$. After reconstruction, axial and coronal slice images through the volumetric micro-CT data were presented for qualitative assessment. The window and level of those images were chosen to highlight the differences in CT numbers between the two respiratory phases.

3. Results

3.1. System performance characterization

3.1.1. MTF analysis. As shown in figure 6, the 10% MTF point was found at 6.2 lp mm^{-1}, which represents a resolution of 81 μm. The 5% MTF point was found at 7.3 lp mm^{-1}, which represents a resolution of 68 μm.

3.1.2. Contrast-to-noise ratio. An axial slice of the contrast phantom is shown in figure 7, with the constituent parts of the phantom labeled as (1) air, (2) water, (3) fat mimic, (4) contrast agent and (5) bone simulator. The average pixel values and standard deviations, in Hounsfield units, from the five material samples, are given in table 1. The CNR between water and air was found to be 10.0 and the CNR between water and oil was found to be 3.7.
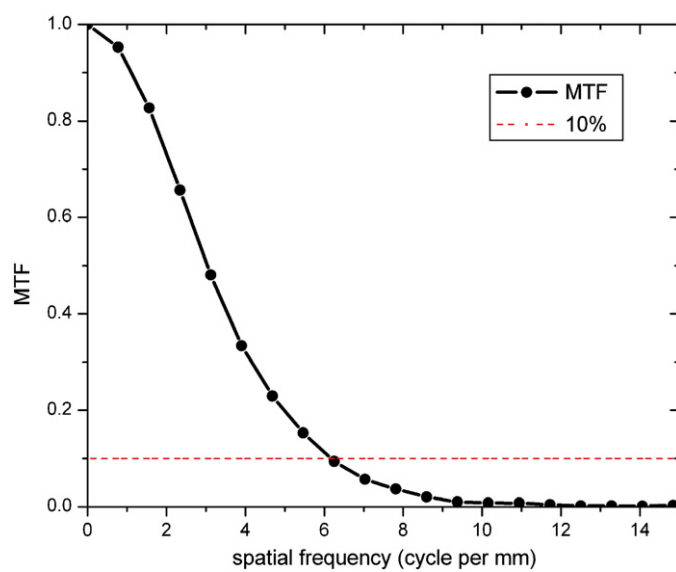
**Figure 6.** The 10% MTF point was found at 6.2 lp mm^{-1}, which represents a resolution of 81 μm.
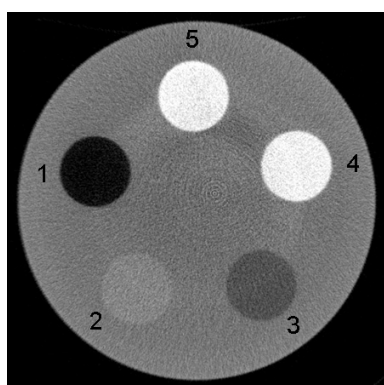
Figure 7. CT slice of the contrast phantom. The constituents of this tissue equivalent phantom are (1) air, (2) water, (3) fat mimic, (4) contrast agent and (5) bone simulator.

Table 1. Averages (μ) and standard deviations (σ), in Hounsfield units, of the pixel values from the ROIs manually place in the center of the various materials shown in figure 7.

	μ	σ
Air	−1000	100
Water	0	100
Fat mimic	−366	97
Contrast agent	1106	130
Bone simulator	1622	196
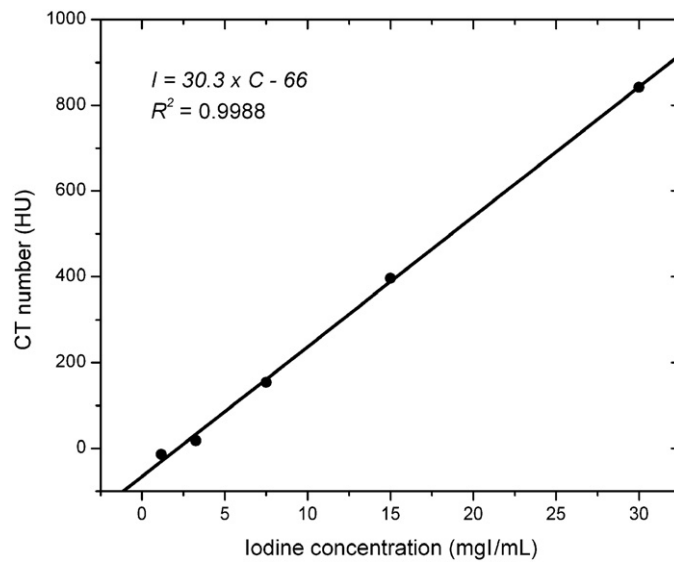
Figure 8. Measured CT number versus iodine solutions of various concentrations, including the results of linear regression. A significant linear correlation is seen between signal intensity and iodine concentration.
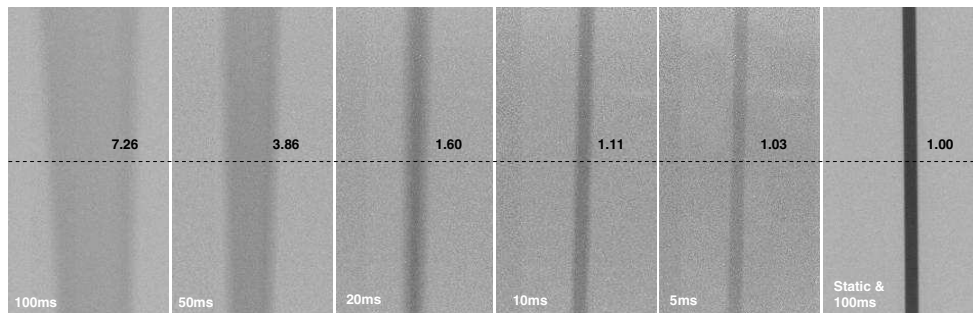
Figure 9. Temporal response of the dynamic micro-CT scanner. Images were taken at 40 kV, 0.7 mA anode current and various x-ray pulse widths. For the reference purpose, shown in the very right is an image taken from single 100 ms x-ray pulse exposure when the wire was static, followed by the images of the moving wire taken at 100 ms, 50 ms, 20 ms, 10 ms and 5 ms pulse width.

3.1.3. Linearity. Linearity of the system was determined from the signal intensities in various concentrations of iodine solutions. Figure 8 shows the signal intensity (I) as a function of increasing iodine concentration (C). Results from linear regression analysis shows the relation follows the equation $I = (30.3 \pm 0.6)$ (HU mL mgI^{-1}) $\cdot C - (66 \pm 9)$ (HU), where C is the iodine concentration in mgI mL^{-1} ($R^2 = 0.9988$). This shows the system is highly linear ($p < 0.0001$). The *y*-intercept value of -66 HU is significantly different from zero, indicating that the scanner calibration may need to be adjusted to account for the beam hardening effect.

3.1.4. Temporal analysis. The x-ray images of the rotating wire phantom taken at various x-ray pulse widths are shown in figure 9. The disc was rotated at the lowest stable rotation speed allowed by the rotor which, when combined with the 115 mm radius of the rotating disk, gives a linear speed of 6.0 (bottom) to 7.5 (top) cm s^{-1} for the part of the wire inside

the scanner's FOV. Every image was the result of a single x-ray pulse exposure. For reference purpose, shown in the very right is an image taken from a 100 ms x-ray pulse exposure when the wire was static. The motion induced blur was clearly visible when the x-ray pulse width was >20 ms, and it could be effectively reduced when the x-ray pulse width was ⩽20 ms. In comparison, for a heart rate of 600 beats per minute and a respiration rate of 120 breaths per minute, the average expansion/contraction speeds of a normal mouse heart and lung are roughly 2 cm s^{-1} (Badea *et al* 2004) and 1 cm s^{-1} (Kiryu *et al* 2008), respectively.

A dashed line is drawn across each image at the center position which has 7 cm s^{-1} translational speed. The full-width at half-maximum (FWHM) of the wire in each image at the dashed line position was measured and scaled to the static reference image, where the FWHM was set to unity. From those normalized FWHM values, we found that imaging blurs resulted from 100 ms, 50 ms, 20 ms, 10 ms and 5 ms exposure of a 1 mm wire moving at 7 cm s^{-1} were at 626%, 286%, 60%, 11% and 3%, respectively. As expected, a shorter x-ray pulse is better in limiting the motion blur, but at the expense of lower signal-to-noise ratio (SNR) due to reduced flux.

The imaging window for respiratory-gated micro-CT of mice was selected at 50 ms and was positioned at the portions of the respiratory cycles where the lung moves as little as possible. The plateaus in the respiration signals were estimated to be about 100 ms. Since the instantaneous moving speeds of the mouse lung is not constant throughout a respiration cycle, a higher temporal resolutions is needed for imaging gated at the parts of the respiration cycles which have faster expansion/contraction speeds, such as the fast contraction phase. The flexibility in choosing the x-ray pulse widths plus the fast gating capability of the CNT-based micro-CT scanner make it relatively easy to perform imaging gated at various respiration phases of mice.

3.1.5. Dose measurement.   The dose for a micro-CT scan using the standard scanning parameters was found to be 11.3 cGy. This dose value is within the range of the dose values reported in literatures for prospectively gated mouse lung micro-CT (Badea *et al* 2004, Namati *et al* 2006, Ford *et al* 2007a, Sera *et al* 2008). Note that in this study there was no filtration on the x-ray source; the x-ray window is a 0.2 mm beryllium foil. The scan dose can be further reduced through the optimization of the x-ray spectrum by filtration.

3.2. Feasibility studies in micro-CT and respiratory-gated micro-CT

3.2.1. Micro-CT of an inflated mouse lung in situ.   An axial slice and a coronal slice from the micro-CT scan of the scarified mouse with inflated lung are shown in figure 10. Images shown have an isotropic voxel size of 31 μm. Small details inside the mouse lung are clearly visible in these images. The CNR between heart and trachea (two gray ROIs in figure 10(a)) was found to be 10.0. The CNR between two types of tissues in heart and chest wall (two white ROIs in figure 10(a)) was found to be 0.5.

3.2.2. Respiratory-gated micro-CT of free-breathing mice.   Figure 11 is a representative result from the respiratory-gated micro-CT of free-breathing mice. The small structures such as vessels and higher order branching airways can be identified in all those images. The lung in the peak inspiration images appear to have a lower CT number than that in the end expiration images. And airways in the peak inspiration images also appear larger in diameter than those in the end expiration images. In the axial images, the artifact around the bones was mainly caused by beam hardening. Beam hardening was expected since no filtration was used in this experiment.
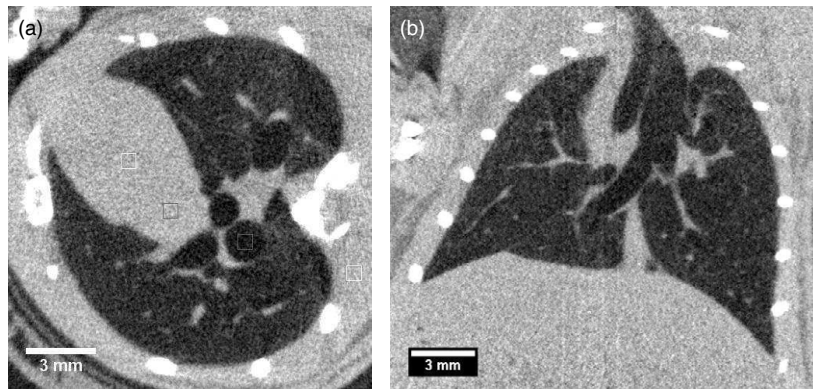
Figure 10. Axial (a) and coronal (b) slices from the micro-CT scan of a scarified mouse with inflated lung. Images shown have an isotropic voxel size of 31 μm. Imaging conditions were 40 kVp, 0.7 mA anode current, 400 ms pulse width, 1 mm aluminum filtration and 325 projections over 195°. The CNR between heart and trachea (two gray ROIs of 20×20 pixels) was determined to be 10.0. The CNR between heart tissue and chest wall tissue (two white ROIs of 20×20 pixels) was determined to be 0.5.
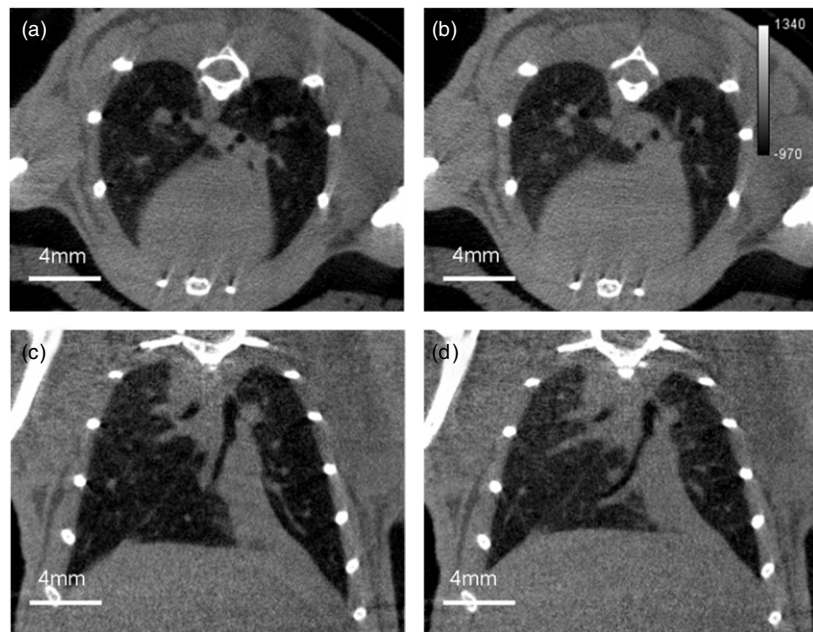
Figure 11. Axial and coronal slice images of the same mouse. Images were reconstructed from two consecutive scans of a single mouse using the same imaging protocol at $62 \times 62 \times 62 \ \mu m^3$ isotropic voxel size. Images shown are from peak inspirations (a) and (c), and end expirations (b) and (d) in the axial and coronal views, respectively. The window and level for these images were chosen to highlight the differences between the two respiratory phases.

4. Discussion

We reported a prototype dynamic micro-CT scanner based on a CNT field emission micro-focus x-ray source. The enabling technology for this scanner is the newly developed CNT-based field emission micro-focus x-ray source. Because emission is electronically rather than thermally driven, x-ray radiation can be readily switched and gated electronically to either periodic or non-periodic signals, which makes the scanner ideal for physiologically gated imaging of free-breathing small animals with rapid motions. At present, the spatial and temporal resolutions of the system are limited at 81 μm and 50 ms, respectively. This is primarily limited by the x-ray flux from the current version of the CNT micro-focus x-ray source.

For the present study, the CNT micro-focus x-ray source was operated at $117 \times 117 \mu$m focal spot size, 40 kVp and 0.7 mA anode current, translating to an x-ray power output of 28 W. Although an exact comparison is difficult to make the overall power output based on the information published in the literature is comparable to the current commercial thermionic micro-focus x-ray tubes. For example, in a recently published study using a modern MicroCAT II scanner (Siemens Preclinical, Knoxville, TN, USA) with a Kevex x-ray source (Thermo Electron Co., Waltham, MA, USA), the micro-focus x-ray tube was reported to operate at 30 W (Namati *et al* 2006).

The output power of a CNT x-ray source is mainly determined by the anode heat load and the cathode current density. An estimation using the empirical relation (Flynn *et al* 1994) of $P_{\max} = 1.4 \times (d_{f,\mathrm{FWHM}})^{0.88}$, for anode voltage $\leqslant 40$ kVp, where $P_{\max}$ is the maximum x-ray tube power in watts and $d_{f,\mathrm{FWHM}}$ is the FWHM of the focal spot in microns, puts the maximum output power of 92 W for continuous tube current at $117 \times 117 \mu$m^2 focal spot size. Therefore, a factor of 3 increase in the tube power is possible while maintaining the same focal spot size, if the current density of the CNT cathode can be increased. The emission current density of the CNT cathode was 0.1 A cm^{-2} in this study. Recent preliminary studies in our lab have shown that field emission at the current density of $\sim$0.5 A cm^{-2} can be obtained with reasonable stability from the CNT cathode with optimized design at the operating conditions used for the micro-CT. Since the present 28 W CNT x-ray tube can put the system temporal and spatial resolutions at 50 ms and 81 μm, respectively, a factor of 3 increase in the x-ray tube power will enable micro-CT imaging with better than 20 ms temporal resolution without sacrificing the SNR and the spatial resolution to perform a high-resolution cardiac-gated imaging. With the x-ray tube operating at a short pulse width and low duty cycle, it is expected that the maximum heat load should be higher thus an even faster temporal resolution can be achieved, although a detailed simulation needs to be performed. Without further increasing the x-ray power, faster than 50 ms temporal resolution can also be achieved with multiple frame acquisition. An undesired consequence of this multiple frame acquisition is the increased scan time.

Limited by the tube current of the present CNT x-ray source, the respiratory-gated mouse lung images in figure 11 were collected without filtration (except 0.2 mm Be window) in order to obtain the high-temporal resolution (50 ms) with a reasonable SNR. We attribute the artifacts around the bones in the axial images to beam hardening. This argument is supported by the result from the inflated lung images in figure 10. In the latter case because we can afford a longer pulse width without degrading the image quality, a 1 mm Al filter was added to reduce the beam hardening effect. As a result, no obvious beam hardening artifact was observed in the reconstructed images. Due to the limit of the tube current from this CNT x-ray source, there is a trade-off between the system MTF, temporal resolution and beam hardening in the imaging quality. Minimizing the beam hardening effect without compromising the system spatial and temporal resolutions requires further increase in the x-ray tube current. We have

recently made progress in this regard. In a preliminary experiment using a different scanner currently under development at UNC, we were able to perform respiratory-gated mouse lung imaging with better filtering. The result is preliminary, but we believe that the dose can be reduced and the beam hardening effect can be minimized. Detailed studies will be discussed in future publications.

As a research prototype, current version of the micro-focus x-ray source has not been fully optimized for a long lifetime. The source was running with heavy use for $\sim$160 days before failure. It should be pointed out that since the emission current and the focal spot size were electronically controlled by the voltages applied to the gate and focusing electrodes, there was no degradation of the performance of the x-ray source or the micro-CT scanner during the entire lifetime. In fact, the focal spot size remained the same without adjusting the focusing voltages even though the gate voltage drifted by $\sim$500 V to maintain the constant emission current. Failure of the x-ray source is due to degradation of the CNT cathode through gradual oxidation of the CNT emitters and occasional arcing events. The total electron beam on time during the lifetime of the source was estimated to be $\sim$20 h. Since the total beam on time required for a typical micro-CT scan is $0.05\,\mathrm{s} \times 325 = 16.25\,\mathrm{s}$, 20 h of beam on time enables a total of 4431 micro-CT scans. With improvement of the CNT cathode and the x-ray source construction, the lifetime of the source can be further improved.

In the current design because the source is housed in a large stationary vacuum chamber, the mouse sample was mounted in the vertical position and rotated to collect the projection images. We have since designed a small ($7 \times 3 \times 3$ inch) and portable version of this source with comparable performance characteristics. This has allowed the construction of a desktop micro-CT scanner with a rotating source and detector pair and a stationary mouse bed. In this configuration, a mouse does not need to be rotated and it can be positioned horizontally. Both are preferred for *in vivo* measurement of the mouse's physiological functions. The portable desktop micro-CT scanner is currently under testing at UNC.

5. Conclusions

In conclusion, we have demonstrated a physiologically gated micro-CT scanner for small animal imaging based on a CNT field emission micro-focus x-ray source. The scanner can readily synchronize its image acquisition to either periodic or non-periodic signals with fast temporal resolution and minimum delay. The 'fire-on-demand' of its timing scheme intrinsically enables a high dose efficiency. The high dose efficiency, high spatial and temporal resolutions of the micro-CT scanner make it ideal for longitudinal studies in free-breathing small animals. This was demonstrated by respiratory-gated micro-CT imaging of several anesthetized free-breathing mice at 50 ms temporal resolution and $6.2\,\mathrm{lp\,mm^{-1}}$ at 10% system MTF using this scanner.

Acknowledgments

References

Badea C, Hedlund L W and Johnson G A 2004 Micro-CT with respiratory and cardiac gating *Med. Phys.* **31** 3324–9

Brown R H, Walters D M, Greenberg R S and Mitzner W 1999 A method of endotracheal intubation and pulmonary functional assessment for repeated studies in mice *J. Appl. Physiol.* **87** 2362–5

Cavanaugh D, Johnson E, Price R E, Kurie J, Travis E L and Cody D D 2004 *In vivo* respiratory-gated micro-CT imaging in small-animal oncology models *Mol. Imaging* **3** 55–62

Cheng Y, Zhang J, Lee Y Z, Gao B, Dike S, Lin W, Lu J and Zhou O 2004 Dynamic radiography using a carbon-nanotube-based field-emission x-ray source *Rev. Sci. Instrum.* **75** 3264

Cody D D, Nelson C L, Bradley W M, Wislez M, Juroske D, Price R E, Zhou X, Bekele B N and Kurie J M 2005 Murine lung tumor measurement using respiratory-gated micro-computed tomography *Invest. ins. Radiol.* **40** 263–9

De Clerck N M, Meurrens K, Weiler H, Van Dyck D, Vanhoutte G, Terpstra P and Postnov A A 2004 High-resolution x-ray microtomography for the detection of lung tumors in living mice *Neoplasia* **6** 374–9

Drangova M, Ford N L, Detombe S A, Wheatley A R and Holdsworth D W 2007 Fast retrospectively gated quantitative four-dimensional (4D) cardiac micro computed tomography imaging of free-breathing mice *Invest. Radiol.* **42** 85–94

European Committee for Standardization M 1999 EN 12543–5 E Brussels

Feldkamp L A, Davis L C and Kress J W 1984 Practical cone-beam algorithm *J. Opt. Soc. Am.* A **1** 612–9

Flynn M, Hames S, Reimann D and Wilderman S 1994 Microfocus x-ray sources for 3D microtomography *Nucl. Instrum. Methods Phys. Res.* A **353** 312–5

Ford N L, Martin E L, Lewis J F, Veldhuizen R A W, Drangova M and Holdsworth D W 2007a *In vivo* characterization of lung morphology and function in anesthetized free-breathing mice using micro-computed tomography *J. Appl. Physiol.* **102** 2046–55

Ford N L, Nikolov H N, Norley C J D, Thornton M M, Foster P J, Drangova M and Holdsworth D W 2005 Prospective respiratory-gated micro-CT of free breathing rodents *Med. Phys.* **32** 2888–98

Ford N L, Wheatley A R, Holdsworth D W and Drangova M 2007b Optimization of a retrospective technique for respiratory-gated high speed micro-CT of free-breathing rodents *Phys. Med. Biol.* **52** 5749–69

Fujita H, Tsai D Y, Itoh T, Doi K, Morishita J, Ueda K and Ohtsuka A 1992 A simple method for determining the modulation transfer function in digital radiography *IEEE Trans. Med. Imaging* **11** 34–9

Gomes R F, Shardonofsky F, Eidelman D H and Bates J H 2001 Respiratory mechanics and lung development in the rat from early age to adulthood *J. Appl. Physiol.* **90** 1631–8

Hedlund L W and Johnson G A 2002 Mechanical ventilation for imaging the small animal lung *ILAR J.* **43** 159–74

Hirai T, McKeown K A, Gomes R F and Bates J H 1999 Effects of lung volume on lung and chest wall mechanics in rats *J. Appl. Physiol.* **86** 16–21

Holdsworth D W and Thornton M M 2002 Micro-CT in small animal and specimen imaging *Trends Biotechnol.* **20** S34–9

Hu J, Haworth S T, Molthen R C and Dawson C A 2004 Dynamic small animal lung imaging via a postacquisition respiratory gating technique using micro-cone beam computed tomography *Acad. Radiol.* **11** 961–70

Kiryu S, Sundaram T, Kubo S, Ohtomo K, Asakura T, Gee J C, Hatabu H and Takahashi M 2008 MRI assessment of lung parenchymal motion in normal mice and transgenic mice with sickle cell disease *J. Magn. Reson. Imaging* **27** 49–56

Kwan A L C, Boone J M, Yang K and Huang S Y 2007 Evaluation of the spatial resolution characteristics of a cone-beam breast CT scanner *Med. Phys.* **34** 275–81

Liu Z, Yang G, Lee Y, Bordelon D, Lu J and Zhou O 2006 Carbon nanotube based microfocus field emission x-ray source for microcomputed tomography *Appl. Phys. Lett.* **89** 103111

Nahrendorf M, Badea C, Hedlund L W, Figueiredo J L, Sosnovik D E, Johnson G A and Weissleder R 2007 High-resolution imaging of murine myocardial infarction with delayed-enhancement cine micro-CT *Am. J. Physiol. Heart Circ. Physiol.* **292** H3172–8

Nakamura T, Malloy J, McCaig L, Yao L J, Joseph M, Lewis J and R V 2001 Mechanical ventilation of isolated septic rat lungs: effects on surfactant and inflammatory cytokines *J. Appl. Physiol.* **91** 811–20

Namati E, Chon D, Thiesse J, Hoffman E A, de Ryk J, Ross A and McLennan G 2006 *In vivo* micro-CT lung imaging via a computer controlled intermittent iso-pressure breath hold (IIBH) technique *Phys. Med. Biol.* **51** 6061–75

Nilsson R 1979 Lung compliance and lung morphology following artificial ventilation in the premature and full-term rabbit neonate *Scand. J. Respir. Dis.* **60** 206–14

Nilsson R, Grossmann G and Robertson B 1980 Artificial ventilation of premature newborn rabbits: effects of positive end-expiratory pressure on lung mechanics and lung morphology *Acta. Paediatr. Scand.* **69** 597–602

Noo F, Clackdoyle R, Mennessier C, White T A and Roney T J 2000 Analytic method based on identification of ellipse parameters for scanner calibration in cone-beam tomography *Phys. Med. Biol.* **45** 3489–508

Oh S J, Zhang J, Cheng Y, Shimoda H and Zhou O 2004 Liquid-phase fabrication of patterned carbon nanotube field emission cathodes *Appl. Phys. Lett.* **87** 3738

Paulus M J, Gleason S S, Kennel S J, Hunsicker P R and Johnson D K 2000 High resolution x-ray computed tomography: an emerging tool for small animal cancer research *Neoplasia* **2** 62–70

Ritman E L 2004 Micro-computed tomography–current status and developments *Annu. Rev. Biomed. Eng.* **6** 185–208

Sera T, Yokota H, Fujisaki K, Fukasaku K, Tachibana H, Uesugi K, Yagi N and Himeno R 2008 Development of high-resolution 4D *in vivo*-CT for visualization of cardiac and respiratory deformations of small animals *Phys. Med. Biol.* **53** 4285–301

Tward D J, Siewerdsena J H, Daly M J, Richard S, Moseley D J, Jaffray D A and Paul N S 2007 Soft-tissue detectability in cone-beam CT: evaluation by 2AFC tests in relation to physical performance metrics *Med. Phys.* **34** 4459–71

Walters E B, Panda K, Bankson J A, Brown E and Cody D D 2004 Improved method of *in vivo* respiratory-gated micro-CT imaging *Phys. Med. Biol.* **49** 4163–72